



Dual hydrogen production from electrocatalytic water reduction coupled with formaldehyde oxidation via a copper-silver electrocatalyst

Received: 14 August 2022

Accepted: 17 January 2023

Published online: 31 January 2023

 Check for updatesGuodong Li¹, Guanqun Han¹, Lu Wang², Xiaoyu Cui¹, Nicole K. Moehring^{3,4,5}, Piran R. Kidambi^{3,4,5}, De-en Jiang^{2,3}  & Yujie Sun¹ 

The broad employment of water electrolysis for hydrogen (H₂) production is restricted by its large voltage requirement and low energy conversion efficiency because of the sluggish oxygen evolution reaction (OER). Herein, we report a strategy to replace OER with a thermodynamically more favorable reaction, the partial oxidation of formaldehyde to formate under alkaline conditions, using a Cu₃Ag₇ electrocatalyst. Such a strategy not only produces more valuable anodic product than O₂ but also releases H₂ at the anode with a small voltage input. Density functional theory studies indicate the H₂C(OH)O intermediate from formaldehyde hydration can be better stabilized on Cu₃Ag₇ than on Cu or Ag, leading to a lower C-H cleavage barrier. A two-electrode electrolyzer employing an electrocatalyst of Cu₃Ag₇(+)||Ni₃N/Ni(-) can produce H₂ at both anode and cathode simultaneously with an apparent 200% Faradaic efficiency, reaching a current density of 500 mA/cm² with a cell voltage of only 0.60 V.

Hydrogen (H₂) is not only an important feedstock in the chemical industry (e.g., petroleum refining, ammonia production from the Haber-Bosch process) but also plays an important role in the future energy economy because H₂ is a carbon-zero energy carrier and can be directly utilized as a fuel in hydrogen fuel cells¹⁻³. Even though mature industry processes exist for the production of H₂, such as steam methane reforming, their strong dependence on unsustainable fossil resources and large CO₂ emission call on greener alternative methods for producing H₂⁴. Against this backdrop, electrocatalytic water splitting, which consists of the H₂ and O₂ evolution reactions (HER and OER), has attracted worldwide attention these years⁵. Despite the great efforts devoted to developing competent electrocatalysts for both half-reactions and ingenious designs of electrolyzers, the thermodynamics of water splitting dictates its large cell voltage input >1.23 V

(Fig. 1a) and hence high-energy consumption (>4.5–6 kWh/m³ H₂)⁶⁻⁹. In fact, the more energy-demanding OER produces O₂ as a low-value product at the anode while H₂ is only produced at the cathode. Therefore, there is an increasing interest in exploring alternative oxidation reactions to replace OER with lower energy input¹⁰. Even more desirable is that value-added products instead of O₂ could be simultaneously obtained at the anode.

Indeed, electrocatalytic oxidation of a variety of inorganic and organic feedstocks has been explored to integrate with HER to produce H₂ with lower voltage input^{11,12}. For instance, our group has reported several electrocatalytic systems to couple the oxidative valorization of various biomass-derived intermediates (e.g., 5-hydroxymethylfurfural (HMF), furfural, etc.) with HER in aqueous media¹³⁻¹⁷. Other small molecules, such as urea^{18,19}, ammonia²⁰, and

¹Department of Chemistry, University of Cincinnati, Cincinnati, OH 45221, USA. ²Department of Chemistry, University of California Riverside, Riverside, CA 92521, USA. ³Department of Chemical and Biomolecular Engineering, Vanderbilt University, Nashville, TN 37212, USA. ⁴Interdisciplinary Graduate Program in Materials Science, Vanderbilt University, Nashville, TN 37235, USA. ⁵Vanderbilt Institute of Nanoscale Science and Engineering, Nashville, TN 37212, USA.

 e-mail: de-en.jiang@vanderbilt.edu; yujie.sun@uc.edu

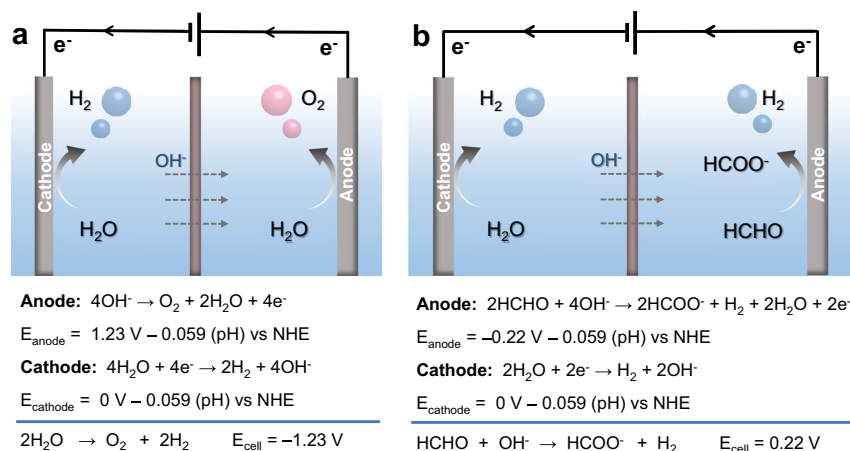


Fig. 1 | Schematic illustration of water electrolysis and HCHO electrooxidation. **a** Conventional electrocatalytic water splitting under alkaline conditions. **b** Electrocatalytic water reduction coupled with HCHO oxidation under alkaline conditions.

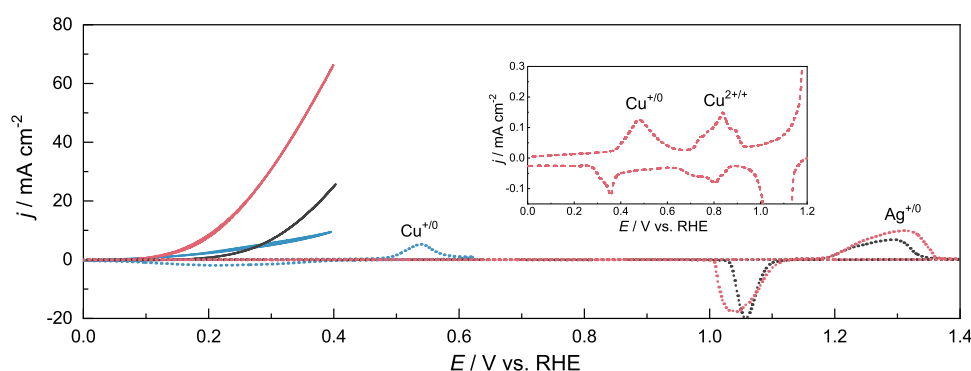


Fig. 2 | HCHO electrooxidation over Cu, Ag, and CuAg catalysts on RDE. CV curves of Cu/RDE (blue), Ag/RDE (black), and Cu_3Ag_7 /RDE (red) in 1.0 M KOH in the absence (dashed) and presence (solid) of 0.6 M HCHO collected at 1500 rpm and 10 mV/s. Inset shows the expanded CV of copper oxidation on Cu_3Ag_7 /RDE.

hydrazine²¹, have also been reported to replace OER for more energy-efficient H_2 production from water, which produces CO_2 and/or N_2 at the anode. Despite the great progress in this direction, H_2 is only produced at the cathode and most electrocatalytic systems still require a cell voltage larger than 1 V to reach an industrially relevant current density ($>500 \text{ mA/cm}^2$). Furthermore, the utilization of biomass-derived feedstocks such as HMF and furfural for the large-scale production of H_2 is still questionable because of the tremendous disparity in their scalability and the future H_2 demand. Consequently, it remains a great challenge to develop an alternative strategy to produce H_2 from water with ultra-low voltage input, and even more desirable is to produce H_2 at both cathode and anode.

We were inspired by the advance in H_2 generation from liquid-phase hydrogen storage molecules, such as NaBH_4 ²², NH_3BH_3 ^{23,24}, and HCOOH ^{25,26}, which are able to release H_2 under thermocatalytic conditions. Among those liquid organic hydrogen storage molecules, formaldehyde (HCHO) is particularly appealing, because the partial HCHO oxidation (FOR) to formate is also able to release H_2 at the anode with a very small thermodynamic potential ($\text{HCHO} + 2\text{OH}^- \rightarrow \text{HCOO}^- + 1/2\text{H}_2 + \text{H}_2\text{O} + \text{e}^-$, $E = -0.22 \text{ V}$ vs. RHE, Fig. 1b)²⁷. Furthermore, HCHO is a low-cost chemical feedstock with a gigantic annual yield while its oxidation product formate (and later formic acid) is a more valuable chemical^{28,29}. Finally, coupling FOR with HER for H_2 production may also provide environmental benefits if toxic formaldehyde residues in wastewater pollutants could be adopted as the feedstock.

Even though H_2 generation from the electrochemical oxidation of HCHO has been reported on a few monometallic electrodes^{30–32}, it remains less explored to couple it with water reduction for dual H_2

production at both anode and cathode. Herein, we report a novel inexpensive electrocatalytic system, Cu_3Ag_7 and $\text{Ni}_3\text{N}/\text{Ni}$ as the anode and cathode electrocatalysts, respectively, to drive FOR and HER under alkaline conditions, which can produce H_2 with an apparent 200% Faradaic efficiency and reach industrially relevant current densities of 100 and 500 mA/cm^2 at cell voltages of only 0.22 and 0.60 V, respectively. Overall, the energy consumption of our two-electrode electrolyzer for H_2 production is merely 0.30 and $0.70 \text{ kWh/m}^3 \text{ H}_2$ at current densities of 100 and 500 mA cm^{-2} , respectively, much lower than the theoretical energy demand of overall water splitting electrolysis ($2.93 \text{ kWh/1 m}^3 \text{ H}_2$).

Results and discussion

Screening of catalysts for formaldehyde oxidation

Inexpensive nitrate salts of copper and silver were utilized as the feedstocks to first prepare the corresponding monometallic electrocatalysts on glassy carbon rotating disk electrode (RDE) via a facile electrodeposition method (see the “Methods” section for details). As shown in Fig. 2, in the absence of HCHO, Cu/RDE showed a well-defined oxidation feature from Cu^0 to Cu^+ at ca. 0.5 V vs. RHE in 1.0 M KOH; while the oxidation peak of Ag^0 to Ag^+ from Ag/RDE did not appear until -1.2 V vs. RHE. Upon the addition of 0.6 M HCHO, an apparent anodic current rise was observed beyond the onset potential (defined at 0.1 mA cm^{-2}) of 0.05 V vs. RHE on Cu/RDE and a current density of 10 mA/cm^2 was obtained at 0.4 V vs. RHE, indicating the electrochemical oxidation of HCHO on Cu/RDE. Despite the more positive onset potential (0.2 V vs. RHE) for HCHO oxidation, a much more rapid current rise was observed on Ag/RDE, which was able to produce an

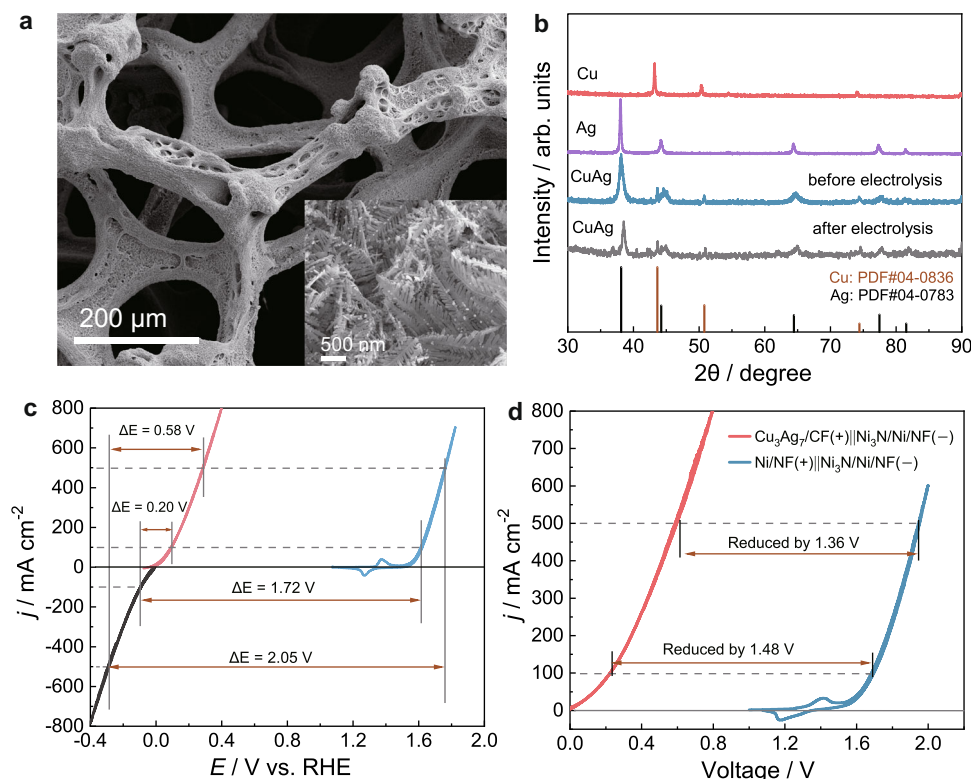


Fig. 3 | Characterizations and HCHO oxidation performances of $\text{Cu}_3\text{Ag}_7/\text{CF}$ electrocatalysts. **a** SEM image of as-prepared $\text{Cu}_3\text{Ag}_7/\text{CF}$. **b** XRD patterns of Cu/CP, Ag/CP, and $\text{Cu}_3\text{Ag}_7/\text{CF}$ prior to and post electrolysis. **c** CV curves of $\text{Cu}_3\text{Ag}_7/\text{CF}$ for HCHO oxidation (red) in 1.0 M KOH with 0.6 M HCHO, $\text{Ni}_3\text{N}/\text{Ni}/\text{NF}$ for HER (black), and Ni/NF for OER (blue) in 1.0 M KOH collected at 10 mV/s. Voltage gaps to reach

100 and 500 mA/cm^2 are indicated. **d** The two-electrode CV curves of HER/FOR (red) and HER/OER (blue) collected at 10 mV/s, in which $\text{Cu}_3\text{Ag}_7/\text{CF}$ and $\text{Ni}_3\text{N}/\text{Ni}/\text{NF}$ were employed as the anode and cathode for the former while Ni/NF and $\text{Ni}_3\text{N}/\text{Ni}/\text{NF}$ for the latter. For FOR, the anolyte was 1.0 M KOH and 0.6 M HCHO while for all the other conditions, 1.0 M KOH was the electrolyte.

anodic current density of 26 mA/cm^2 at 0.4 V RHE. The differences in onset potential and the anodic current rise of HCHO oxidation on Cu/RDE versus Ag/RDE prompted us to finely tune the ratio between Cu and Ag precursors in electrodeposition, aiming to synthesize a bimetallic CuAg electrocatalyst with optimized activity.

As shown in Supplementary Fig. 1, by systematically varying the Cu/Ag ratio from 9/1 to 1/9 (see the Supplementary Information for electrodeposition details), all the bimetallic CuAg/RDE electrodes possess similar electrochemical double layer capacitances ($C_{dl} = 0.7\text{--}0.8\text{ mF}/\text{cm}^2$), close to those of the pristine monometallic samples (0.5–0.6 mF/cm^2). Therefore, these bimetallic CuAg/RDE samples have similar electrochemical active surface area, which allows a fair comparison of their electrocatalytic activity of HCHO oxidation based on the measured geometric current density. Supplementary Fig. 2a plots the cyclic voltammograms (CVs) of all the CuAg/RDE samples as well as Cu/RDE and Ag/RDE measured under the same condition (0.6 M HCHO in 1.0 M KOH). It is apparent that $\text{Cu}_3\text{Ag}_7/\text{RDE}$ exhibited the best performance (Supplementary Fig. 2b). The ICP-MS analysis result of $\text{Cu}_3\text{Ag}_7/\text{RDE}$ confirmed the Cu/Ag ratio was 3:7. Therefore, all the subsequent electrochemical HCHO oxidation studies were carried out using Cu_3Ag_7 as the optimal electrocatalyst.

In the absence of HCHO, $\text{Cu}_3\text{Ag}_7/\text{RDE}$ still retained the typical copper redox features of Cu^{+0} and $\text{Cu}^{2+/+}$ between 0.4 and 1.0 V vs. RHE but with suppressed current density (Fig. 2 inset) relative to that of Cu/RDE in 1.0 M KOH. Further positive scanning revealed an analogous oxidation feature of Ag^0 to Ag^+ beyond 1.2 V vs. RHE as observed for Ag/RDE. The addition of 0.6 M HCHO resulted in a drastic anodic current rise starting at ca 0.1 V vs. RHE, which was able to reach 66 mA/cm^2 at 0.4 V vs. RHE (Fig. 2), substantially higher than those obtained on monometallic Cu/RDE (10 mA/cm^2) and Ag/RDE (26 mA/cm^2) at the same potential.

Using $\text{Cu}_3\text{Ag}_7/\text{RDE}$ as a model electrode, we investigated the impact of HCHO concentration on the obtained current density (Supplementary Fig. 3) and it was found that 0.6 M HCHO produced the maximum current density at 0.4 V vs. RHE in 1.0 M KOH. Increasing the HCHO concentration beyond 0.6 M resulted in decreased anodic current, likely due to more disproportionation of HCHO at higher concentrations (Cannizzaro reaction)³³. Next, the impact of OH^- concentration was also probed and the results were compiled in Supplementary Fig. 4. In 1.0 M NaClO_4 , no anodic current was observed on $\text{Cu}_3\text{Ag}_7/\text{RDE}$ between 0 and 0.4 V vs. RHE when 0.1 M HCHO was added. However, a slight increase to 1 mM $[\text{OH}^-]$ was able to produce a noticeable anodic current at 0.4 V RHE. A higher HCHO oxidation current was observed along the increase in $[\text{OH}^-]$. Overall, these results demonstrate that an alkaline condition is necessary for the electrochemical oxidation of HCHO on $\text{Cu}_3\text{Ag}_7/\text{RDE}$.

Electrolysis performances

With the optimal Cu/Ag ratio in hand, we next sought to electrodeposit Cu_3Ag_7 on highly porous and conductive substrates for electrolysis studies. To avoid the introduction of other metal composites, commercially available copper foam was adopted as the catalyst support and current collector. A slightly modified electrodeposition approach was utilized to prepare Cu_3Ag_7 on copper foam (CF) and the resulting electrode was named $\text{Cu}_3\text{Ag}_7/\text{CF}$ (see the “Methods” section for details). The scanning electron microscopy (SEM) image of a pristine copper foam indicates its porous skeleton with a smooth surface (Supplementary Fig. 5a). After the electrodeposition of Cu_3Ag_7 , the as-prepared $\text{Cu}_3\text{Ag}_7/\text{CF}$ shows nearly complete coverage of the copper foam by pine needle-like electrodeposits (Fig. 3a and Supplementary Fig. 5b). Energy-dispersive X-ray spectroscopy analysis (EDX) of $\text{Cu}_3\text{Ag}_7/\text{CF}$ resulted in a Cu/Ag ratio very close to 3:7 (Supplementary

Fig. 5c, d), in agreement with the ICP-MS results of $\text{Cu}_3\text{Ag}_7/\text{RDE}$. To shed light on the crystallinity of electrodeposited Cu_3Ag_7 , X-ray diffraction was performed. In this case, carbon paper (CP), instead of copper foam, was used as the catalyst support, in order to avoid the interference of the background signal from the copper foam. The obtained XRD patterns of Cu/CP , Ag/CP , and $\text{Cu}_3\text{Ag}_7/\text{CP}$ included in Fig. 3b confirmed that the bimetallic sample consists of both crystalline Cu (JCPDS Card no. 04-0836) and Ag (JCPDS Card no. 04-0783)^{34,35}. The most prominent peaks at around 44° and 38° are corresponding to the (111) facets of Cu and Ag, respectively, which are preserved in $\text{Cu}_3\text{Ag}_7/\text{CP}$. To further investigate the structure of $\text{Cu}_3\text{Ag}_7/\text{CF}$, high-resolution transmission electron microscopy (HRTEM) combined with selected area electron diffraction (SAED) was performed. Supplementary Fig. 6a presents a clear dendritic structure in line with the SEM images (Fig. 3a and Supplementary Fig. 5c). The HRTEM images (Supplementary Fig. 6b, c) show the well-resolved lattice fringes with an inter-planar distance of 0.237 and 0.208 nm corresponding to the (111) crystal planes of cubic Ag and Cu, respectively. The distinct diffraction rings from SAED (Supplementary Fig. 6d) demonstrate the polycrystalline nature and could be indexed to the (111), (200), (220), and (311) planes of Ag and Cu³⁶, respectively, in good agreement with the XRD results. High-angle-annular dark-field STEM (HAADF-TEM) and EDX element mapping images reveal a uniform distribution of Cu and Ag throughout the dendrites (Supplementary Fig. 6e).

Next, a two-compartment electrochemical cell (H-cell) with an anion exchange membrane was used to investigate the electrochemical HCHO oxidation on $\text{Cu}_3\text{Ag}_7/\text{CF}$. As shown in Fig. 3c, the CV curve of $\text{Cu}_3\text{Ag}_7/\text{CF}$ collected in 1.0 M KOH with 0.6 M HCHO presents a nearly zero onset potential and very steep anodic current increase, reaching 100 and 500 mA/cm^2 at merely 0.10 and 0.28 V vs. RHE, respectively. In sharp contrast, when electrodeposited nickel nanoparticles on nickel foam (Ni/NF) were employed as the OER electrocatalysts, much higher potentials (1.62 and 1.76 V vs. RHE) were required to reach the same current densities (100 and 500 mA/cm^2). We previously reported an excellent earth-abundant HER electrocatalyst composed of interfaced Ni_3N and Ni on nickel foam ($\text{Ni}_3\text{N}/\text{Ni}/\text{NF}$) in 1.0 M KOH³⁷. For the sake of comparison, we also included the CV curve of $\text{Ni}_3\text{N}/\text{Ni}/\text{NF}$ for the cathodic H_2 evolution in Fig. 3c. With the above CVs, we were able to deduce that the voltage inputs for HER coupled with FOR would be much smaller to reach industrially relevant current densities like 100 and 500 mA/cm^2 , requiring only 0.20 and 0.58 V, respectively, when $\text{Cu}_3\text{Ag}_7/\text{CF}$ and $\text{Ni}_3\text{N}/\text{Ni}/\text{NF}$ were employed as the anode and cathode electrocatalysts, respectively. However, much larger voltages were demanded ($>1.7\text{V}$) for water splitting (HER/OER) to produce the same current density when using the Ni/NF (anode) and $\text{Ni}_3\text{N}/\text{Ni}/\text{NF}$ (cathode) catalyst couple. Indeed, as plotted in Fig. 3d, when a two-electrode electrolyzer of FOR/HER was assembled using $\text{Cu}_3\text{Ag}_7/\text{CF}$ as the anode and $\text{Ni}_3\text{N}/\text{Ni}/\text{NF}$ as the cathode, the corresponding CV curve collected in 1.0 M KOH with 0.6 M HCHO only required cell voltages of 0.22 and 0.60 V to deliver the current densities of 100 and 500 mA/cm^2 , respectively, yet much higher cell voltages of 1.70 and 1.96 V were needed for conventional water splitting electrolysis. In short, this FOR/HER strategy using the $\text{Cu}_3\text{Ag}_7/\text{CF}(\text{+})/\text{Ni}_3\text{N}/\text{Ni}/\text{NF}(\text{-})$ electrode couple exhibited great superiority compared to reported systems of HER integrated with the oxidation of various inorganic and organic feedstocks (Table S1), in terms of applied voltage and Faradaic efficiency for H_2 production.

Products analysis

Since the commercially purchased HCHO (37 wt% in H_2O) contains methanol as a stabilizer and HCHO oxidation will produce formate under alkaline conditions, it is of critical importance to determine if $\text{Cu}_3\text{Ag}_7/\text{CF}$ can catalyze the oxidation of methanol and formate within this small potential window. CV of $\text{Cu}_3\text{Ag}_7/\text{RDE}$ from 0 to 0.4 V vs. RHE in 1.0 M KOH was first collected after the addition of 0.1 M formic acid,

0.1 M methanol, and 0.1 M HCHO, respectively. As shown in Supplementary Fig. 7, the increase in anodic current on $\text{Cu}_3\text{Ag}_7/\text{RDE}$ was negligible upon the addition of either methanol or formic acid. However, a rapid anodic current rise was observed once HCHO was added, indicating that $\text{Cu}_3\text{Ag}_7/\text{RDE}$ could effectively catalyze the electrooxidation of HCHO but not formic acid or methanol within this potential region, likely due to the smaller bond dissociation energy of C–H bond in H-CHO ($88.0 \pm 0.2 \text{ kcal mol}^{-1}$) compared to all the bonds in methanol and formic acid³⁸.

Figure 4a presents the chronoamperometry curve of $\text{Cu}_3\text{Ag}_7/\text{CF}$ in 1.0 M KOH upon the continuous addition of 0.1 M formic acid, 0.1 M methanol, and 0.1 M HCHO. It is apparent that negligible anodic current increase was observed upon the addition of either formic acid or methanol with a voltage input of 0.6 V, indicating that $\text{Cu}_3\text{Ag}_7/\text{CF}$ was not able to catalyze their electrochemical oxidation with this small voltage. In contrast, the addition of 0.1 M HCHO led to an immediate anodic current rise to 230 mA/cm^2 . These results prove that $\text{Cu}_3\text{Ag}_7/\text{CF}$ possesses an excellent selectivity towards the electrochemical oxidation of HCHO with low voltage input, which is not affected by the presence of methanol and formate.

Gas chromatography was also performed to confirm (Supplementary Fig. 8) and quantify the amount of produced gas from the H-cell where $\text{Cu}_3\text{Ag}_7/\text{CF}$ was employed as the anode and $\text{Ni}_3\text{N}/\text{Ni}/\text{NF}$ as the cathode in a two-electrode configuration. As shown in Fig. 4b, without applied voltage, no H_2 was detected, suggesting that $\text{Cu}_3\text{Ag}_7/\text{CF}$ was not able to thermocatalytically drive HCHO oxidation in 1.0 M KOH with 0.6 M HCHO at room temperature. Along with the increase of voltage input from 0.2 to 0.8 V, because of the faster H_2 production rate, continuously decreased electrolysis time was needed to produce 2 mmol H_2 from the anode chamber. Comparing the experimentally measured amount of H_2 and the calculated amount of H_2 based on passed charge during each electrolysis of different voltage inputs (0.2–0.8 V) confirmed that 100% Faradaic efficiency (FE) was achieved for anodic H_2 production within the entire voltage range (Fig. 4b inset and Supplementary Fig. 9). In the meantime, cathodic H_2 production from the $\text{Ni}_3\text{N}/\text{Ni}/\text{NF}$ cathode was also able to produce H_2 with a 100% FE. For instance, Fig. 4c overlaps the measured H_2 amounts over the theoretical H_2 amounts along the passed charge for both cathode and anode chambers during electrolysis carried out at 0.8 V when 1.0 M KOH with 0.6 M HCHO was used as the anolyte and 1.0 M KOH as the catholyte. The nearly perfect alignment of the H_2 amounts for both chambers confirmed that 100% FE of H_2 production was realized for both electrodes and collectively 200% FE for overall H_2 generation.

The organic products in the liquid phase of the anode chamber were determined and quantified to assess the carbon balance of electrolysis. The amounts of methanol and formate were determined from ^1H NMR measurements using *t*-butanol as an internal standard (Supplementary Fig. 10). Besides the quantity resulting from the Cannizzaro reaction, all the additional formate was produced from the electrochemical HCHO oxidation (Supplementary Fig. 11 and Table S2). As shown in Fig. 4d, 100% FE of formate production was achieved for five consecutive 1 h controlled-current electrolysis (150 mA) using the $\text{Cu}_3\text{Ag}_7/\text{CF}$ and $\text{Ni}_3\text{N}/\text{Ni}/\text{NF}$ couple but fresh electrolyte for each cycle. In the meantime, 200% FE of overall H_2 production was retained for all five cycles as well. Further, the remaining HCHO was quantified via UV–vis absorption measurement following the Hantzsch reaction (see the “Methods” section for details)³⁹, using a pre-established calibration curve (Supplementary Fig. 12). From the results (Supplementary Fig. 13 and Table S2) we conclude that 100% carbon balance of HCHO was maintained for the above five consecutive electrolysis cycles using the same electrode couple.

The stability of the $\text{Cu}_3\text{Ag}_7/\text{CF}$ and $\text{Ni}_3\text{N}/\text{Ni}/\text{NF}$ electrode couple was further tested by both chronopotentiometry and chronoamperometry electrolysis. Figure 4e shows nearly identical chronopotentiometric curves for five consecutive controlled-current

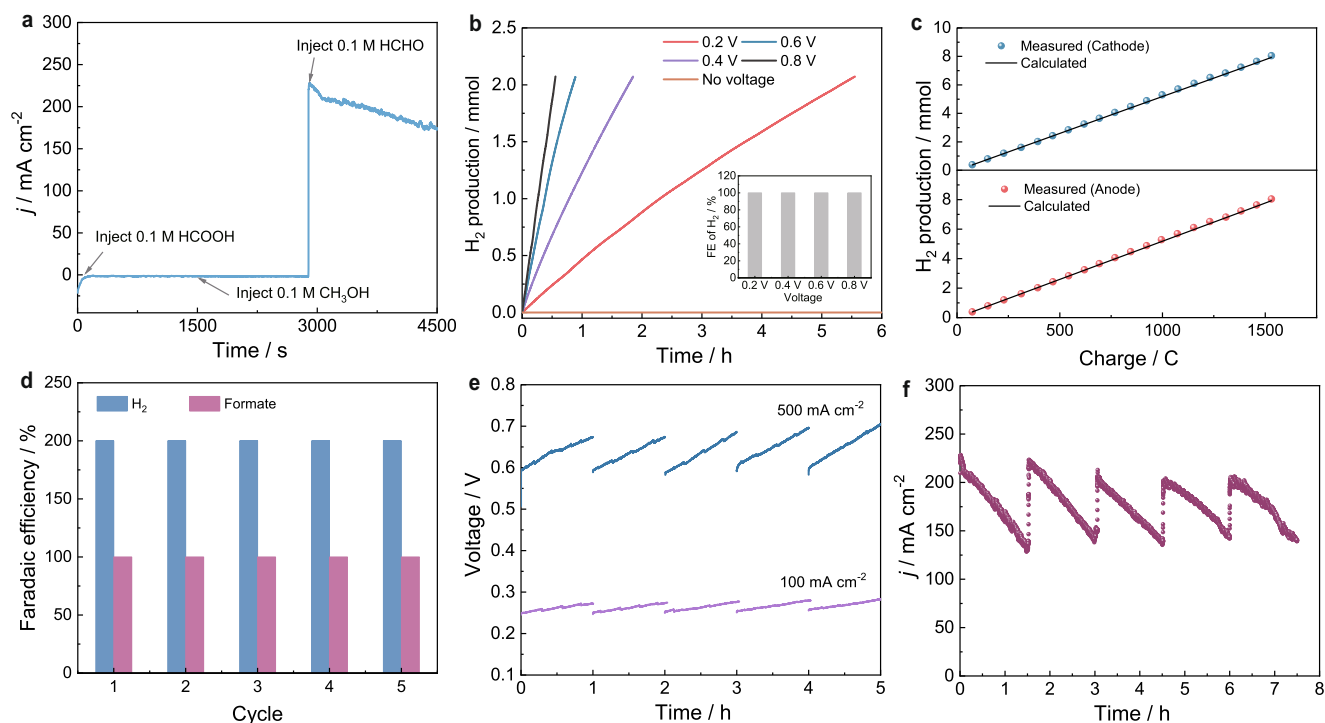


Fig. 4 | Dual hydrogen production of FOR/HER system. The electrolysis experiments were conducted in a two-electrode electrolyzer using $\text{Cu}_3\text{Ag}_7/\text{CF}$ anode and $\text{Ni}_3\text{N}/\text{Ni}/\text{NF}$ cathode. **a** Chronoamperometric curve collected at a cell voltage of 0.6 V in 1.0 M KOH with the continuous addition of 0.1 M HCOOH, 0.1 M CH_3OH , and 0.1 M HCHO in the anode chamber. **b** Comparison of the experimentally measured amount of H_2 from the anode chamber with different voltage inputs. Inset shows the Faradaic efficiency of H_2 production. **c** Comparison of the experimentally measured H_2 amounts with the theoretical H_2 amounts calculated from

the passed charge for both cathode and anode chambers during electrolysis at a cell voltage of 0.6 V. **d** Faradaic efficiencies of H_2 and formate production for five consecutive 1 h controlled-current (150 mA) electrolysis cycles.

e Chronopotentiometric curves for five consecutive controlled-current electrolysis cycles conducted at 100 and 500 mA/cm^2 . **f** Chronoamperometric curves at a cell voltage of 0.6 V with the periodic replenishment of fresh HCHO back to its original 0.1 M concentration in anolyte.

electrolysis conducted at 100 and 500 mA/cm^2 in a fresh anolyte (1.0 M KOH and 0.6 M HCHO) of each cycle using the same electrode couple. In addition, a 7.5 h chronoamperometry experiment was carried out in the same electrolyte at a cell voltage of 0.6 V with the periodic replenishment of fresh HCHO back to its original 0.1 M concentration. Immediate resume of the anodic current was observed for each period (Fig. 4f). Post-electrolysis characterization of $\text{Cu}_3\text{Ag}_7/\text{CF}$ displayed negligible changes in morphology, crystallinity, and electrochemical double-layer capacitance (Fig. 3b and Supplementary Figs. 14, 15). Overall, these results corroborate the superior structural robustness and mechanical stability of $\text{Cu}_3\text{Ag}_7/\text{CF}$ for long-term electrochemical HCHO oxidation for anodic H_2 production with low voltage input.

Theoretical computations

To shed light on the improved performance of the bimetallic $\text{Cu}_3\text{Ag}_7/\text{CF}$ relative to monometallic Cu/CF and Ag/CF in the anodic H_2 production from electrocatalytic HCHO oxidation, density functional theory (DFT) computation was performed to examine the structure and energetics of key steps during FOR. Because only a small voltage is needed to drive FOR, one can assume that the electrocatalytic reaction proceeds close to the thermodynamic limit. Under thermal conditions, the commonly accepted mechanism of FOR is that HCHO first becomes hydrated and deprotonated in the alkaline solution to yield the $\text{H}_2\text{C}(\text{OH})\text{O}^-$ anion, which then adsorbs on the catalyst surface^{40,41}. The resulting $\text{H}_2\text{C}(\text{OH})\text{O}^*$ intermediate is dehydrogenated via C-H cleavage to yield HCOOH^* and H^* (Fig. 5a), which is a key step we focus on. Our experimental characterization showed that the (111) facets are preferentially exposed for the Cu, Ag, and Cu_3Ag_7 catalysts, so we used the (111) surfaces to compare the three catalysts (see Supplementary Fig. 16a for the details of the models). First, we compared the relative

adsorption energy of the $\text{H}_2\text{C}(\text{OH})\text{O}^*$ intermediate: as shown in Fig. 5b, adsorption on Cu_3Ag_7 is most preferred, with the O group anchored at the Cu_2Ag_1 hollow site; the top view shows a clear staggered conformation of the H_2COH group relative to the Cu_2Ag_1 site (Fig. 5c), distinct from the more eclipsed conformations on $\text{Cu}(111)$ and $\text{Ag}(111)$ (Supplementary Fig. 16b). Analysis of the projected density of states of the anchored O group of $\text{H}_2\text{C}(\text{OH})\text{O}^*$ at the Cu_2Ag_1 site indicates that there are strong orbital mixings of O 2p states with Cu 3d states from -1.5 to -1.0 eV as well as with Ag 4d states from -6 to -5 and -4 to -3 eV (Supplementary Fig. 16c). In other words, the existence of the separate two d-bands on the bimetallic surface provides more flexibility in adsorbing and stabilizing the $\text{H}_2\text{C}(\text{OH})\text{O}^*$ intermediate. Indeed, C-H cleavage is much more facile on Cu_3Ag_7 from the staggered adsorption conformation (Fig. 5d). After C-H cleavage, the formation of H_2 from two H^* was found to be facile as well on Cu_3Ag_7 (Fig. 5e): the energy barrier is 0.66 eV, which is expected to be further lowered when entropy is taken into account. To complete the reaction, HCOOH^* will desorb from the surface and then deprotonate to form formate in the solution.

Electrocatalytic paraformaldehyde oxidation and energy efficiency analysis

The promising activity of Cu_3Ag_7 towards HCHO oxidation to produce H_2 , corroborated by our DFT results, prompted us to further expand the substrate scope. Especially, we were motivated to explore the possibility of utilizing paraformaldehyde as the feedstock for the following reasons. In contrast to HCHO aqueous solutions with limited concentration (e.g., 37 wt%) and containing methanol as the stabilizer, paraformaldehyde is solid under ambient conditions, possessing much higher mass density and also lower cost⁴². It is known that HCHO can

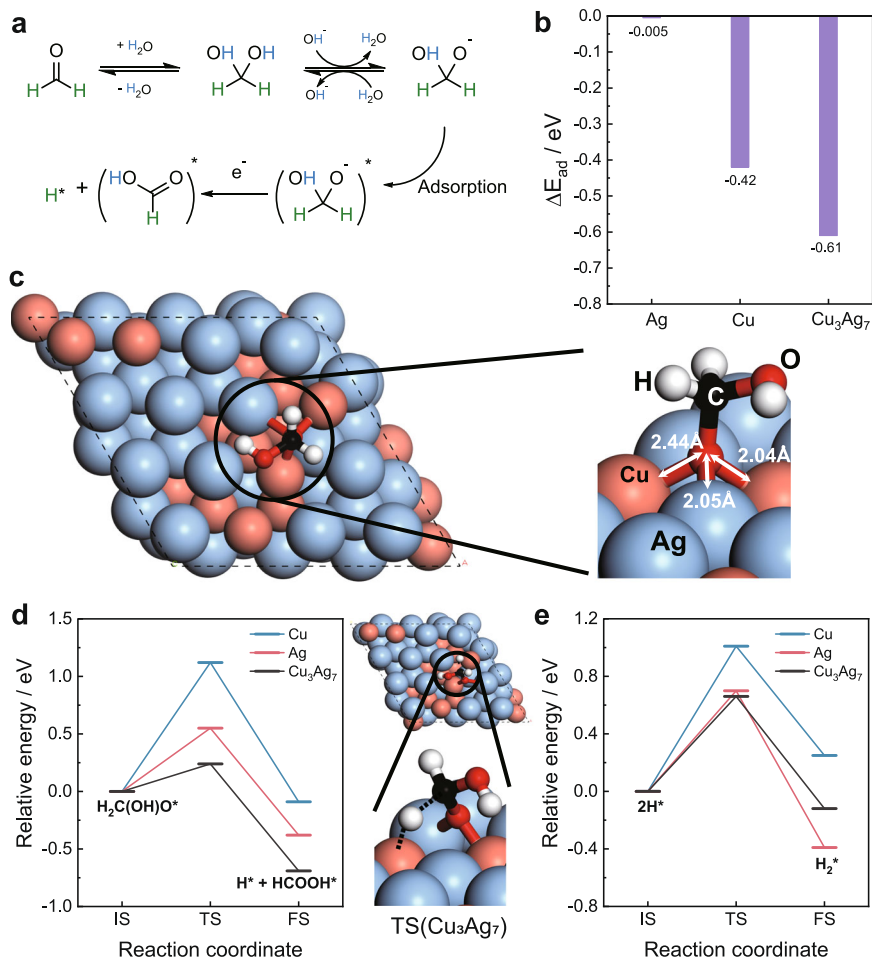


Fig. 5 | DFT theoretical computations. **a** Proposed mechanism of HCHO oxidation to HCOOH. **b** Computed adsorption energy of the H₂C(OH)O intermediate on the three model surfaces. **c** Optimized adsorption geometry of H₂C(OH)O on Cu₃Ag₇.

d Initial (IS), transition (TS), and final (FS) states of H₂C(OH)O dehydrogenation on the three model surfaces, together with the TS structure on Cu₃Ag₇. **e** H₂ formation via the Tafel step on the three surfaces.

be released from paraformaldehyde when dissolved in an aqueous solution⁴³. To our delight, as shown in Supplementary Fig. 17a, Cu₃Ag₇/RDE still exhibited excellent electrocatalytic activity for the oxidation of paraformaldehyde, superior to Cu/RDE and Ag/RDE. Concentration dependence experiments indicated that 10.0 g/L paraformaldehyde resulted in the highest oxidation current density (60 mA/cm²) on Cu₃Ag₇/RDE in 1.0 M KOH (Supplementary Fig. 17b). Figure 6a compares the CV curves collected on Cu₃Ag₇/CF and Ni/NF in the presence and absence of 10.0 g/L paraformaldehyde, respectively. It is apparent that much smaller potentials of 0.13 and 0.36 V vs. RHE are required to produce 100 and 500 mA/cm², respectively, than those required for OER on Ni/NF. Nearly unity Faradaic efficiencies were obtained for both H₂ and formate production when paraformaldehyde was employed as the feedstock and Cu₃Ag₇/CF as the anode electrocatalyst at different applied potentials from 0.1 to 0.4 V vs. RHE (Fig. 6b, Supplementary Figs. 8b and 18, and Table S3). Notably, when paraformaldehyde was used as the oxidation substrate, the yields of methanol and formate from the competing Cannizzaro reaction were much lower than those directly using HCHO solutions, suggesting another advantage of using paraformaldehyde as the feedstock for our dual HER strategy. The long-term stability test of electrolysis using paraformaldehyde was also carried out using a flow cell consisting of AEM and Ni₃N/Ni/NF(-)||Cu₃Ag₇/CF(+) electrode couple in a zero-gap configuration. The electrolysis was performed at 100 mA cm⁻² with 1.0 M KOH as the catholyte and 1.0 M KOH plus 10.0 g/L paraformaldehyde as the anolyte, both of which were fed into the cell at a

flow rate of 50 mL min⁻¹. The electrolyte was refreshed every 24 h. Supplementary Fig. 19 demonstrates that our dual H₂ production strategy (HER/FOR) using the Ni₃N/Ni/NF(-)||Cu₃Ag₇/CF(+) electrode couple can maintain a low voltage input (0.4–0.6 V without iR correction) to deliver 100 mA cm⁻² over 260 h, indicating the great robustness of our electrocatalysts for dual H₂ production.

From an energy efficiency perspective, our dual H₂ production system surpasses those conventional water-splitting systems to a substantial extent. For instance, Fig. 6c compares the electricity consumption between our dual H₂ production strategy (HER/FOR) using the Ni₃N/Ni/NF(-)||Cu₃Ag₇/CF(+) electrode couple and traditional water electrolysis (HER/OER) using the Ni₃N/Ni/NF(-)||Ni/NF(+) electrode couple. To produce H₂ at a current density of 100 mA/cm², our dual H₂ production system only requires 0.30 kWh of electricity per m³ H₂ whereas conventional water splitting demands 4.10 kWh. Even at an industrially applicable current density of 500 mA/cm², the electricity consumption of our dual H₂ production system is still as small as 0.70 kWh/m³ H₂, much lower than that of water electrolysis (4.70 kWh/m³ H₂).

In summary, we report a bimetallic electrocatalyst Cu₃Ag₇ for efficient H₂ production at the anode of an electrolyzer which integrates the partial oxidation of formaldehyde with water reduction to realize dual HER with an apparent 200% Faradaic efficiency. DFT computation reveals a key adsorption conformation of the H₂C(OH)O* intermediate on Cu₃Ag₇ that is highly conducive to C–H cleavage. In addition to formaldehyde solution, solid-phase paraformaldehyde can be equally

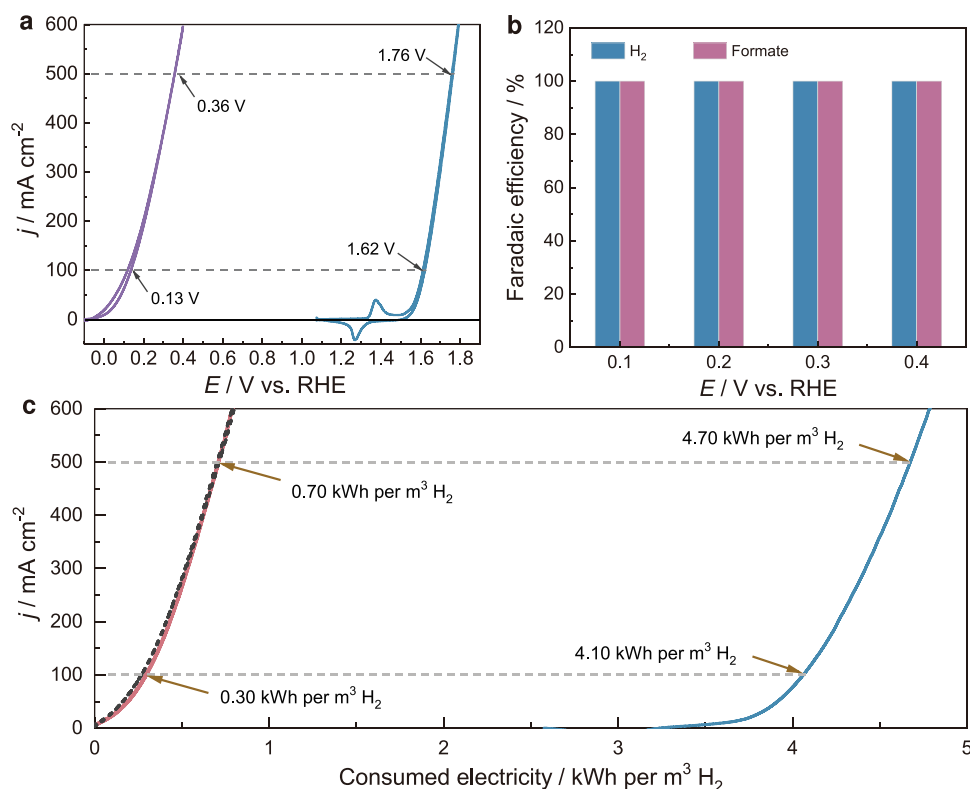


Fig. 6 | Electrocatalytic paraformaldehyde oxidation and energy efficiency analysis. **a** CV curves of $\text{Cu}_3\text{Ag}_7/\text{CF}$ (red) in 1.0 M KOH with 10.0 g/L paraformaldehyde and Ni/NF (blue) in 1.0 M KOH collected at 10 mV/s. **b** Faradaic efficiencies of H_2 and formate production in the anode chamber during each electrolysis at different potentials using $\text{Cu}_3\text{Ag}_7/\text{CF}$ as the anode, 1.0 M KOH as the

catholyte, and 1.0 M KOH with 10.0 g/L paraformaldehyde as the analyte. **c** Comparative analysis of the calculated electricity consumption for H_2 production between our formaldehyde (red) or paraformaldehyde (black) oxidation-integrated strategy using the $\text{Ni}_3\text{N}/\text{Ni}/\text{NF}(-)\|\text{Cu}_3\text{Ag}_7/\text{CF}(+)\|$ electrode couple and traditional water electrolysis (HER/OER) using the $\text{Ni}_3\text{N}/\text{Ni}/\text{NF}(-)\|\text{Ni}/\text{NF}(+)\|$ electrode couple.

employed as a reactant to realize similar performance, paving the way for practical application on a large scale.

Methods

Chemicals

All chemicals were used as received without any further purification. Copper(II) nitrate hydrate, silver nitrate, copper(II) sulfate pentahydrate, silver sulfate, potassium hydroxide (>85%), formaldehyde solution (37 wt% in H_2O), paraformaldehyde, formic acid (>99%), methanol (>99.9%), tert-butanol (anhydrous), hydrochloric acid (ACS reagent, 37%), sodium citrate were purchased from Sigma Aldrich. Ammonium chloride and nickel(II) chloride hexahydrate were purchased from Alfa Aesar. Copper foam and nickel foam with a purity >99.99% were purchased from MTI. Deionized water (18 M Ω cm) from a Barnstead E-Pure system was used in all experiments.

Synthesis

Synthesis of Cu, Ag, and CuAg catalysts on rotating disk electrode.

The catalysts were synthesized through a convenient and straightforward electrodeposition method by using a typical three-electrode system on a VMP-3 potentiostat (Biologic Science Instrument). A rotating disk electrode with glassy carbon (RDE, 0.196 cm^2 , Pine Research Instrumentation) was used as the working electrode with a leakless Ag/AgCl (eDAQ) reference electrode and a Pt mesh counter electrode. -0.2 V vs. Ag/AgCl was applied to the RDE working electrode for the reduction of Cu and Ag ions in the electrolyte. The electrodeposition ended when a charge of 60 mC had been passed. Cu modified on RDE (Cu/RDE) and Ag modified on RDE (Ag/RDE) were electrodeposited at -0.2 V vs. Ag/AgCl from an aqueous electrolyte containing specific amounts of $\text{Cu}(\text{NO}_3)_2$ (20.0 mM, 30 mL)

and AgNO_3 (20.0 mM, 30 mL), respectively. For comparison, the $\text{Cu}_x\text{Ag}_{10-x}/\text{RDE}$ ($x=1, 3, 5, 7$, and 9) were prepared under the same conditions from precursor electrolytes (20.0 mM, 30.0 mL) containing AgNO_3 and $\text{Cu}(\text{NO}_3)_2$ solutions with different concentration ratios (from 1/9 to 9/1).

Synthesis of Cu_3Ag_7 catalysts on Cu foam ($\text{Cu}_3\text{Ag}_7/\text{CF}$)

To avoid the introduction of other metal composites, copper foam (0.5 cm \times 0.5 cm) was used as the catalyst support and current collector. The copper foam was sequentially washed with 1.0 M HCl, ethanol, and deionized water (each for 10 min). $\text{Cu}_3\text{Ag}_7/\text{CF}$ was synthesized through electrodeposition on a Gamry Interface 1000 electrochemical workstation with a three-electrode configuration, using a carbon rod and a leakless Ag/AgCl (eDAQ) electrode as the counter electrode and reference electrode, respectively. $\text{Cu}_3\text{Ag}_7/\text{CF}$ was electrodeposited at a constant current of -3.0 A cm^{-2} for 30 s from an aqueous electrolyte (30 mL) containing specific amounts of Ag_2SO_4 (14.0 mM) and CuSO_4 (6.0 mM) in 1.5 M H_2SO_4 under Ar without stirring. In addition, 0.1 M sodium citrate was added to the precursor as a complexing agent. To avoid the interference of the background signal from copper foam in the XRD tests, we prepared Cu-modified, Ag-modified, and Cu_3Ag_7 -modified carbon paper electrodes (Cu/CP, Ag/CP, and $\text{Cu}_3\text{Ag}_7/\text{CP}$) samples following the same preparation conditions. The only difference is that copper foam was replaced by carbon paper.

Synthesis of Ni/NF and $\text{Ni}_3\text{N}/\text{Ni}/\text{NF}$

Based on our previous work³⁷, the $\text{Ni}_3\text{N}/\text{Ni}/\text{NF}$ electrode was synthesized from the electrodeposition of Ni particles on a nickel foam followed by thermal nitridation. A piece of clean nickel foam

(0.5 cm × 0.5 cm) was used as the working electrode. A carbon rod was used as the counter electrode. The Ni/NF was synthesized through electrodeposition at a constant current density of -1.0 A cm^{-2} for 500 s in a two-electrode cell containing NiCl_2 (0.1 M) and NH_4Cl (2.0 M) under Ar without stirring. The $\text{Ni}_3\text{N}/\text{Ni}/\text{NF}$ was obtained from the thermal annealing of Ni/NF under an NH_3 flow at 300 °C for 6 h with a ramping rate of $10 \text{ }^\circ\text{C min}^{-1}$.

Physical characterization

The morphology features of samples were assessed by using scanning electron microscopy (FEI XL30, 15 kV), as well as transmission electron microscopy (TEM), selective area electron diffraction (SAED, 40 μm aperture), and scanning transmission electron microscopy (STEM) with an FEI Tecnai Osiris (200 kV). Samples for TEM were prepared by suspending dry $\text{Cu}_3\text{Ag}_7/\text{CF}$ electrocatalyst on carbon-coated 200-mesh copper TEM grids (Ted Pella 01894-F). STEM-energy-dispersive X-ray spectroscopy (EDX) maps were collected using Bruker Esprit 1.9 software and averaged over 8 scans. X-ray diffraction (XRD) patterns were collected on a Philips X'Pert Pro PW3040/00 (PAN analytical) instrument. The scan range was set from 20° to 90° (in 2θ) with a Cu-tube operated at 45 kV and 40 mA. The evolved H_2 through the electrolysis process was quantified by gas chromatography (GC, SRI 8610C) equipped with a Molecular Sieve 13 packed column, a Hayes-Sep D packed column, and a thermal conductivity detector, and Ar was used as the carrier gas. The Cu and Ag quantities of the sample were analyzed via inductively coupled plasma mass spectrometry (ICP-MS, Agilent 7700 series) in 2% nitric acid. ^1H NMR spectra were recorded in the designated solvents on a Bruker AV 400 MHz spectrometer. UV-vis absorption spectra were collected on an Agilent 8454 UV-Vis Spectrophotometer.

Electrochemical measurements

All catalysts on RDE were tested on an electrochemical workstation (VMP-3 potentiostat, Biologic Science Instrument) with a modulated speed rotator (PINE Research Instrumentation) at room temperature in a standard three-electrode configuration. An RDE (0.196 cm^2) was utilized as the working electrode, while a Pt mesh and a Hg/HgO (1.0 M KOH) electrode were used as the counter electrode and reference electrode, respectively. All potentials herein were referenced to the reversible hydrogen electrode (RHE) through calibration via Pt foil as the working electrode in the H_2 -saturated electrolyte. All potentials measured in 1.0 M KOH were converted to the value versus RHE according to the equation: $E_{\text{RHE}} = E_{\text{Hg/HgO}} + 0.924 \text{ V}$. Commercial formaldehyde (37 wt%) solution was directly used as the oxidation substrate. The Cu/RDE, Ag/RDE, and $\text{Cu}_x\text{Ag}_{10-x}/\text{RDE}$ were treated using cyclic voltammetry (CV) from 0 to $0.3 V_{\text{RHE}}$ at 50 mV s^{-1} for 20 cycles to obtain metallic Cu or Ag in 1.0 M KOH under Ar prior to the HCHO electrooxidation (FOR) test (Supplementary Fig. 20). All CVs of FOR were performed in the electrolyte under Ar at a scan rate of 10 mV s^{-1} and a rotation rate of 1500 rpm without iR correction in a standard three-electrode configuration. For investigating the effect of $[\text{OH}^-]$, 1.0 M anion concentration anolyte consisted of NaOH and NaClO_4 with different concentrations to avoid the interference of conductivity change. All potentials herein were referenced to the reversible hydrogen electrode (RHE) through calibration using Pt foil as the working electrode in H_2 -saturated electrolytes with different OH^- concentrations. The electrochemical double-layer capacitance (C_{dl}) measurements were performed using cyclic voltammetry, which was collected in a non-Faradaic region with various scan rates ranging from 20 to 200 mV s^{-1} at potentials between 0.07 and 0.17 V vs. RHE in 1.0 M KOH under Ar. For paraformaldehyde oxidation on RDE, all experimental procedures were the same as FOR.

The measurements of FOR on $\text{Cu}_3\text{Ag}_7/\text{CF}$, HER on $\text{Ni}_3\text{Ni}/\text{Ni}/\text{NF}$, and OER on Ni/NF were conducted on the VMP-3 potentiostat in an H-cell with an anion exchange membrane (Fumasep FAA-3-50), using a

Pt mesh as the counter electrode and a Hg/HgO (1.0 M KOH) as the reference electrode, respectively. $\text{Cu}_3\text{Ag}_7/\text{CF}$ was treated using cyclic voltammetry from 0 to $0.3 V_{\text{RHE}}$ at 50 mV s^{-1} for 20 cycles to obtain metallic Cu or Ag in 1.0 M KOH under Ar prior to the HCHO electrooxidation test. All CVs (FOR, HER and OER) in a three-electrode configuration were collected at a scan rate of 10 mV s^{-1} without iR correction. The two-electrode electrolysis was performed on an electrochemical workstation in H-cell with an anion exchange membrane. For conventional water electrolysis, the Ni/NF and $\text{Ni}_3\text{Ni}/\text{Ni}/\text{NF}$ were employed as the anode and cathode in 1.0 M KOH, respectively. For a two-electrode electrolyzer of FOR/HER, $\text{Cu}_3\text{Ag}_7/\text{CF}$ was the anode and $\text{Ni}_3\text{Ni}/\text{Ni}/\text{NF}$ was the cathode, in which 1.0 M KOH and 0.6 M HCHO were used as the anolyte and 1.0 M KOH as the catholyte. The uncompensated resistance (R_u) of 1.0 M KOH in the absence or presence of HCHO was determined by the Current Interrupt (CI) method of a VMP-3 potentiostat and the value of R_u was measured as $15 \pm 0.2 \Omega$. All CVs in a two-electrode configuration were collected under Ar at a scan rate of 10 mV s^{-1} with iR compensation by the automatic CI method with a value of $90\% \times R_u$ through the EC-lab software. For the gas products analysis from the anode chamber, different cell voltages (0.2–0.8 V) were applied for chronoamperometry where $\text{Cu}_3\text{Ag}_7/\text{CF}$ was employed as the anode and $\text{Ni}_3\text{Ni}/\text{Ni}/\text{NF}$ as the cathode in a two-electrode configuration. The Faradaic efficiency analysis of H_2 and formate production in the cathode and anode chambers was performed from five consecutive 1 h controlled-current electrolysis (150 mA) using the $\text{Cu}_3\text{Ag}_7/\text{CF}$ and $\text{Ni}_3\text{Ni}/\text{Ni}/\text{NF}$ couple but fresh electrolyte for each cycle. The chronopotentiometry test was performed by five consecutive controlled-current electrolysis conducted at 100 and 500 mA cm^{-2} in a fresh anolyte (1.0 M KOH and 0.6 M HCHO) of each cycle using the $\text{Ni}_3\text{Ni}/\text{Ni}/\text{NF}(-)|\text{Cu}_3\text{Ag}_7/\text{CF}(+)$ electrode couple. The chronoamperometry measurement was carried out at a cell voltage of 0.6 V with the periodic replenishment of fresh HCHO back to its original 0.1 M concentration. For the electrocatalytic paraformaldehyde oxidation on $\text{Cu}_3\text{Ag}_7/\text{CF}$, all experimental procedures were the same as FOR. The long-term stability test was carried out in a homemade flow cell with serpentine flow channels ($1 \text{ cm} \times 1 \text{ cm}$) using $\text{Cu}_3\text{Ag}_7/\text{CF}$ as the anode and $\text{Ni}_3\text{Ni}/\text{Ni}/\text{NF}$ as the cathode on a Biologic VMP-3 potentiostat without iR-compensation. The catholyte (1.0 M KOH) and anolyte (1.0 M KOH and 10.0 g/L PFA) were fed into the cell at a flow rate of 50 mL min^{-1} by a peristaltic pump (Peri-Star Pro Peristaltic Pump, World Precision Instruments) and recycled. The electrolyte was refreshed every 24 h. An anion exchange membrane (Fumasep FAA-3-50) was used to separate the anolyte and catholyte.

Product analysis

The evolved H_2 in both anode chamber and cathode chamber of a two-electrode electrolyzer of FOR/HER was analyzed by gas chromatography (GC, SRI 8610C) equipped with a Molecular Sieve 13 packed column, a HayesSep D packed column, and a thermal conductivity detector. The oven is kept at 80 °C using Ar as carrier gas. The quantity of H_2 production was determined via a water displacement method.

The concentration of formaldehyde during electrolysis was quantified via UV-vis absorption measurement following the Hantzsch reaction³⁹. Ammonium acetate (15.4 g) in water (50 mL), glacial acetic acid (0.3 mL), and acetylacetone (0.2 mL) were mixed to form a solution under stirring, which was further diluted with water (49.5 mL). To measure the concentration of formaldehyde, 20.0 μL of anolyte was acidified by 20 μL 2.0 M HCl and then diluted 2500 times prior to and post-electrolysis. Subsequently, 2.0 mL of the diluted solution was mixed with the acetylacetone solution (2.0 mL), which was further heated to 60 °C for 10 min. After cooling for 10 min, the absorbance of the sample solution at 413 nm was measured. The quantification of HCHO was obtained from the calibration curves by applying standard solutions with known concentrations of commercially purchased pure HCHO.

The identification and quantification of formic acid and methanol were determined from the ^1H NMR using calibration curves with *t*-butanol (10.0 mM) as an internal standard. 100 μL electrolyte from anolyte and catholyte prior to and post electrolysis was acidified by 20 μL HCl (37%) and then added into 500 μL D_2O . ^1H NMR was recorded using a water suppression method.

The Faradaic efficiency was calculated on the basis of the following equation:

$$\text{FE (\%)} = (nF \times N / Q_{\text{total charge passed}}) \times 100 \quad (1)$$

where n is the number of electrons transferred for each product molecule, F is Faraday's constant ($96,485 \text{ C mol}^{-1}$), N is the mole number of products and Q is the total passed charge.

The carbon balance (%) of the electrooxidation process was calculated using the following equation:

$$\text{carbon balance (\%)} = \frac{\text{mol of organic products}}{\text{mol of formaldehyde consumed}} \times 100 \quad (2)$$

Theoretical computation

Density functional theory (DFT) calculations were performed by using Vienna Ab initio Simulation Package (VASP)^{44,45}. The Perdew–Burke–Ernzerhof (PBE) functional within the generalized gradient approximation (GGA) was used for electron exchange correlation⁴⁶. Projector augmented wave (PAW) potential was used to treat the nuclei-electron interaction^{47,48}. An energy cutoff of 400 eV was chosen for plane wave basis sets. The atomic positions were relaxed until the force on each atom was $<0.05 \text{ eV/\AA}$. Electronic energies converged within 10^{-4} eV . Transition states were searched using the Climbing Image Nudged Elastic Band approach^{49,50}. Frequency analysis was carried out to ensure that there was only a single imaginary frequency for the transition state.

The bulk model of Cu_3Ag_7 was built based on the bulk model of Ag. Starting with a $2 \times 2 \times 2$ supercell of bulk Ag with 16 Ag atoms, we replaced two Ag atoms with Cu and obtained four different geometries for $\text{Cu}_2\text{Ag}_{14}$. After optimization, the lowest energy structure was used as a starting structure to generate six different geometries for $\text{Cu}_3\text{Ag}_{13}$ from replacing one Ag in $\text{Cu}_2\text{Ag}_{14}$ with Cu. Repeating the optimization and the single-atom substitution of the lowest-energy structure, seven geometries of $\text{Cu}_4\text{Ag}_{12}$ and two geometries of $\text{Cu}_5\text{Ag}_{11}$ were tested and compared. In total, over 20 bulk geometries were examined for a stable structure for $\text{Cu}_5\text{Ag}_{11}$ (Cu/Ag = 0.45) which was used to approximate the bulk Cu_3Ag_7 (Cu/Ag = 0.43) composition. A slab with five layers in a (3×3) lateral supercell was built for Cu_3Ag_7 , Ag, and Cu (111) surfaces and sampled by $2 \times 2 \times 1$ k -point mesh. The bottom two layers were fixed, and the other atoms were all relaxed during the structural optimization. The vacuum layer was set to be 15 Å. Coordinates for the bulk model and the (111) surface of the bimetallic system are provided in Supplementary Data 1.

Data availability

All data are available in the manuscript, the supplementary materials and from the authors on request. Source data are provided as a Source Data file. Source data are provided with this paper.

References

- Jacobson, M. Z., Colella, W. G. & Golden, D. M. Cleaning the air and improving health with hydrogen fuel-cell vehicles. *Science* **308**, 1901–1905 (2005).
- United States Department of Energy. *A National Vision of America's Transition to a Hydrogen Economy-to 2030 and Beyond* (United States Department of Energy, 2003).
- International Energy Agency (IEA). *The Future of Hydrogen* (International Energy Agency (IEA), 2019).
- Turner, J. A. Sustainable hydrogen production. *Science* **305**, 972–974 (2004).
- Chatenet, M. et al. Water electrolysis: from textbook knowledge to the latest scientific strategies and industrial developments. *Chem. Soc. Rev.* **51**, 4583–4762 (2022).
- Wang, J. et al. Non-precious-metal catalysts for alkaline water electrolysis: operando characterizations, theoretical calculations, and recent advances. *Chem. Soc. Rev.* **49**, 9154–9196 (2020).
- Zhu, J., Hu, L., Zhao, P., Lee, L. Y. S. & Wong, K. Y. Recent advances in electrocatalytic hydrogen evolution using nanoparticles. *Chem. Rev.* **120**, 851–918 (2020).
- Lagadec, M. F. & Grimaud, A. Water electrolyzers with closed and open electrochemical systems. *Nat. Mater.* **19**, 1140–1150 (2020).
- Zhang, L., Wang, Z. & Qiu, J. Energy-saving hydrogen production by seawater electrolysis coupling sulfion degradation. *Adv. Mater.* **34**, 2109321 (2022).
- You, B. & Sun, Y. Innovative strategies for electrocatalytic water splitting. *Acc. Chem. Res.* **51**, 1571–1580 (2018).
- You, B., Han, G. & Sun, Y. Electrocatalytic and photocatalytic hydrogen evolution integrated with organic oxidation. *Chem. Commun.* **54**, 5943–5955 (2018).
- Li, R., Xiang, K., Peng, Z., Zou, Y. & Wang, S. Recent advances on electrolysis for simultaneous generation of valuable chemicals at both anode and cathode. *Adv. Energy Mater.* **11**, 2102292 (2021).
- You, B., Jiang, N., Liu, X. & Sun, Y. Simultaneous H_2 generation and biomass upgrading in water by an efficient noble-metal-free bifunctional electrocatalyst. *Angew. Chem. Int. Ed.* **55**, 9913–9917 (2016).
- You, B., Liu, X., Jiang, N. & Sun, Y. A General strategy for decoupled hydrogen production from water splitting by integrating oxidative biomass valorization. *J. Am. Chem. Soc.* **138**, 13639–13646 (2016).
- Jiang, N., You, B., Boonstra, R., Terrero Rodriguez, I. M. & Sun, Y. Integrating electrocatalytic 5-hydroxymethylfurfural oxidation and hydrogen production via Co–P-derived electrocatalysts. *ACS Energy Lett.* **1**, 386–390 (2016).
- Jiang, N. et al. Electrocatalysis of furfural oxidation coupled with H_2 evolution via nickel-based electrocatalysts in water. *ChemNanoMat* **3**, 491–495 (2017).
- You, B., Liu, X., Liu, X. & Sun, Y. Efficient H_2 evolution coupled with oxidative refining of alcohols via a hierarchically porous nickel bifunctional electrocatalyst. *ACS Catal.* **7**, 4564–4570 (2017).
- Forslund, R. P., Alexander, C. T., Abakumov, A. M., Johnston, K. P. & Stevenson, K. J. Enhanced electrocatalytic activities by substitutional tuning of nickel-based ruddlesden–popper catalysts for the oxidation of urea and small alcohols. *ACS Catal.* **9**, 2664–2673 (2019).
- Chen, W. et al. Unveiling the electrooxidation of urea: intramolecular coupling of the N–N bond. *Angew. Chem. Int. Ed.* **60**, 7297–7307 (2021).
- Zhang, M. et al. An efficient symmetric electrolyzer based on bifunctional perovskite catalyst for ammonia electrolysis. *Adv. Sci.* **8**, 2101299 (2021).
- Zhu, Y. et al. Dual nanoislands on Ni/C hybrid nanosheet activate superior hydrazine oxidation-assisted high-efficiency H_2 production. *Angew. Chem. Int. Ed.* **61**, e202113082 (2022).
- Zhang, X. et al. Efficient hydrogen generation from the NaBH_4 hydrolysis by cobalt-based catalysts: positive roles of sulfur-containing salts. *ACS Appl. Mater. Interfaces* **12**, 9376–9386 (2020).
- Wang, Q. et al. Dramatic synergy in CoPt nanocatalysts stabilized by “click” dendrimers for evolution of hydrogen from hydrolysis of ammonia borane. *ACS Catal.* **9**, 1110–1119 (2018).

24. Fu, F. et al. Highly selective and sharp volcano-type synergistic Ni₂Pt@ZIF-8-catalyzed hydrogen evolution from ammonia borane hydrolysis. *J. Am. Chem. Soc.* **140**, 10034–10042 (2018).
25. Choi, B.-S. et al. Core-shell engineering of Pd-Ag bimetallic catalysts for efficient hydrogen production from formic acid decomposition. *ACS Catal.* **9**, 819–826 (2018).
26. Li, S. J. et al. A simple and effective principle for a rational design of heterogeneous catalysts for dehydrogenation of formic acid. *Adv. Mater.* **31**, 1806781 (2019).
27. Ken-ichi, M. & Michio, E. Formaldehyde electro-oxidation on copper metal and copper-based amorphous alloys in alkaline media. *Bull. Chem. Soc. Jpn.* **58**, 2043–2050 (1985).
28. Trincado, M., Grützmacher, H. & Precht, M. H. G. CO₂-based hydrogen storage—hydrogen generation from formaldehyde/water. *Phys. Sci. Rev.* **3**, 20170013 (2018).
29. Bulushev, D. A. & Ross, J. R. H. Towards sustainable production of formic acid. *ChemSusChem* **11**, 821–836 (2018).
30. Meerakker, J. E. A. M. V. D. On the mechanism of electroless plating. I. Oxidation of formaldehyde at different electrode surfaces. *J. Appl. Electrochem.* **11**, 387–393 (1981).
31. Beltowska-Brzezinska, M. Electrochemical oxidation of formaldehyde on gold and silver. *Electrochim. Acta* **30**, 1193–1198 (1985).
32. Beltowska-Brzezinska, M. & Heitbaum, J. On the anodic oxidation of formaldehyde on Pt, Au and Pt/Au-alloy electrodes in alkaline solution. *J. Electroanal. Chem.* **183**, 167–181 (1985).
33. Martin, R. J. L. The mechanism of the Cannizzaro reaction of formaldehyde. *Aust. J. Chem.* **7**, 335–347 (1954).
34. Dutta, A., Rahaman, M., Luedi, N. C., Mohos, M. & Broekmann, P. Morphology matters: tuning the product distribution of CO₂ electroreduction on oxide-derived Cu foam catalysts. *ACS Catal.* **6**, 3804–3814 (2016).
35. Dutta, A., Morstein, C. E., Rahaman, M., Cedeño López, A. & Broekmann, P. Beyond copper in CO₂ electrolysis: effective hydrocarbon production on silver-nanofoam catalysts. *ACS Catal.* **8**, 8357–8368 (2018).
36. Deo Malviya, K., Srivastava, C. & Chattopadhyay, K. Phase formation and stability of Ag-60 at%Cu alloy nanoparticles synthesized by chemical routes in aqueous media. *Phys. Chem. Chem. Phys.* **19**, 28006–28013 (2017).
37. Song, F. et al. Interfacing nickel nitride and nickel boosts both electrocatalytic hydrogen evolution and oxidation reactions. *Nat. Commun.* **9**, 4531 (2018).
38. Blanksby, S. J. & Ellison, G. B. Bond dissociation energies of organic molecules. *Acc. Chem. Res.* **36**, 255–263 (2003).
39. Nash, T. The colorimetric estimation of formaldehyde by means of the Hantzsch reaction. *Biochem. J.* **55**, 416–421 (1953).
40. Kapoor, S., Barnabas, F. A., Sauer, M. C., Meisel, D. & Jonah, C. D. Kinetics of hydrogen formation from formaldehyde in basic aqueous-solutions. *J. Phys. Chem.* **99**, 6857–6863 (1995).
41. ten Kortenaar, M. V., Kolar, Z. I., de Goeij, J. J. M. & Frens, G. Adsorption, exchange, and oxidation of formaldehyde on gold: a radiotracer study. *Langmuir* **18**, 10279–10291 (2002).
42. Fetzer, M. N. A., Tavakoli, G., Klein, A. & Precht, M. H. G. Ruthenium-catalyzed e-selective partial hydrogenation of alkynes under transfer-hydrogenation conditions using paraformaldehyde as hydrogen source. *ChemCatChem* **13**, 1317–1325 (2021).
43. Suenobu, T., Isaka, Y., Shibata, S. & Fukuzumi, S. Catalytic hydrogen production from paraformaldehyde and water using an organoiridium complex. *Chem. Commun.* **51**, 1670–1672 (2015).
44. Kresse, G. & Furthmüller, J. Efficiency of ab-initio total energy calculations for metals and semiconductors using a plane-wave basis set. *J. Comput. Mater. Sci.* **6**, 15–50 (1996).
45. Kresse, G. Efficient iterative schemes for ab initio total-energy calculations using a plane-wave basis set. *Phys. Rev. B* **54**, 11169–11186 (1996).
46. Perdew, J. P., Burke, K. & Ernzerhof, M. Generalized gradient approximation made simple. *Phys. Rev. Lett.* **77**, 3865–3868 (1996).
47. Blochl, P. E., Jepsen, O. & Andersen, O. K. Improved tetrahedron method for Brillouin-zone integrations. *Phys. Rev. B* **49**, 16223–16233 (1994).
48. Kresse, G. & Joubert, D. From ultrasoft pseudopotentials to the projector augmented-wave method. *Phys. Rev. B* **59**, 1758–1775 (1999).
49. Henkelman, G. & Jónsson, H. Improved tangent estimate in the nudged elastic band method for finding minimum energy paths and saddle points. *J. Chem. Phys.* **113**, 9978 (2000).
50. Henkelman, G., Uberuaga, B. P. & Jónsson, H. A climbing image nudged elastic band method for finding saddle points and minimum energy paths. *J. Chem. Phys.* **113**, 9901–9904 (2000).

Acknowledgements

Y.S. acknowledges the support of the National Science Foundation (CHE-1914546 and CHE-2102220) and Herman Frasch Foundation (820-HF17). DFT computation (D.J.) was sponsored by the National Science Foundation (CHE-2102191).

Author contributions

Y.S. conceived and designed this research. G.L. and G.H. synthesized and characterized the catalysts and performed electrocatalysis experiments. L.W. and D.J. conducted the theoretical computation. G.L. and X.C. carried out the ICP-MS measurements. N.K.M. and P.R.K. performed TEM and HR-TEM measurements. All authors contributed to the analysis and interpretation of the results. G.L., Y.S., and D.J. wrote the manuscript.

Competing interests

Y.S. has filed a provisional patent application related to this manuscript (US patent provisional 63/440,048). All other authors declare no competing interests.

Additional information

Supplementary information The online version contains supplementary material available at <https://doi.org/10.1038/s41467-023-36142-7>.

Correspondence and requests for materials should be addressed to De-en Jiang or Yujie Sun.

Peer review information *Nature Communications* thanks the anonymous reviewers for their contribution to the peer review of this work. Peer reviewer reports are available.

Reprints and permissions information is available at <http://www.nature.com/reprints>

Publisher's note Springer Nature remains neutral with regard to jurisdictional claims in published maps and institutional affiliations.

Open Access This article is licensed under a Creative Commons Attribution 4.0 International License, which permits use, sharing, adaptation, distribution and reproduction in any medium or format, as long as you give appropriate credit to the original author(s) and the source, provide a link to the Creative Commons license, and indicate if changes were made. The images or other third party material in this article are included in the article's Creative Commons license, unless indicated otherwise in a credit line to the material. If material is not included in the article's Creative Commons license and your intended use is not permitted by statutory regulation or exceeds the permitted use, you will need to obtain permission directly from the copyright holder. To view a copy of this license, visit <http://creativecommons.org/licenses/by/4.0/>.

© The Author(s) 2023